

Bio-Inspired Pneumatic Modular Actuator for Peristaltic Transport

Brian Ye*, Zhuonan Hao*, Priya Shah, Mohammad Khalid Jawed[†]

Abstract—Peristalsis, a biologically inspired mechanism, plays a crucial role in locomotion and material transport in living systems. While extensively studied in nature, its application in soft robotics for handling and transporting objects has seen progress but remains limited. This study presents a pneumatic modular actuator, fabricated from silicone polymer, that is scalable, adaptable, and repairable in situ. The system integrates donut-shaped actuation modules capable of radial and axial inflation, coupled with real-time pressure feedback for synchronized control across multiple stacked modules. Experimental validation demonstrates the actuator’s ability to grasp and transport objects with diameters as small as 0.4 times its inner diameter at a speed of $2.08 \pm 0.07 \text{ mm/s}$. The system successfully handles a range of object materials, including deformable soft tubes, solid handheld levels, and irregularly shaped bundles of pens. This work advances peristaltic actuation on object transportation, enabling safe and reliable manipulation of deformable and irregularly shaped materials across various applications, such as underwater specimen delivery and field robotics operations.

Index Terms—Bio-inspired system, peristaltic transport, soft robotics, pneumatic actuator

I. INTRODUCTION

PERISTALSIS, defined as the involuntary, wave-like contraction and relaxation of circular and longitudinal muscles [1], is a widespread biological mechanism essential for various functions in animals and humans. It primarily enables locomotion and facilitates the transport of substances such as food, fluids, and waste. On one hand, soft-bodied animals, such as earthworms, sea cucumbers, snails, and certain types of fish, use peristalsis for locomotion [2]. They rely on wave-like muscular elongation and contraction along their bodies to propel themselves through their environment [3], such as soil, water, or along surfaces. On the other hand, peristalsis is fundamental for biological organisms to transport solid or liquid substances [4], facilitated by the propagation of rhythmic contraction waves along tubular structures [5], such as the esophagus, stomach, intestines, and ureter [6]. The process provides slow but stable [7] and adaptable transportation [8],

minimizing energy consumption [9] and enabling movement through small or irregular openings [10] while maintaining functionality under varying conditions [11].

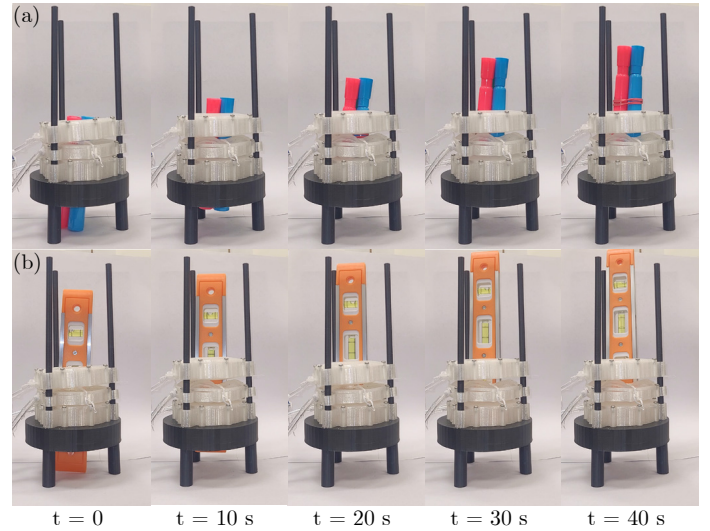


Fig. 1: Demonstration of the actuator’s capability to transport irregular objects using a fundamental unit with three stacked modules: (a) a bundle of marker pens and (b) a handheld leveling tool.

With recent advancements in soft robotics, researchers have increasingly focused on developing soft robots and bio-inspired systems that replicate biological mechanisms and behaviors [12], [13]. To leverage the benefits of a soft, compliant body and the peristalsis mechanism, worm-like crawling robots have been developed using various actuation, fabrication, and control methods [14]. These studies highlight the advantages of the peristaltic mechanism, including its adaptability to diverse environments, high compliance, and fault tolerance, ensuring reliability in complex systems. However, most existing works focus on locomotion rather than object transport applications. In particular, studies on peristaltic transport system often center on monolithic devices for biological applications. For example, Dirven et al. [15] developed a pneumatically actuated peristaltic device made from silicone rubber, which mimics esophageal swallowing and enables continuous, compliant transport through occlusive pressure waves. Likewise, Pend et al. [16], [17] created a pneumatic, large intestine-inspired soft robot that uses McKibben muscles for axial and circumferential contractions, facilitating object transport via traveling waves. In a similar vein, Uzawa et al. [18] and Kawano et al. [19] proposed the peristaltic transport system for space toilets that uses

Manuscript received: November 30, 2024; Revised: March 10, 2025; Accepted: May 30, 2025. This paper was recommended for publication by Editor Cecilia Laschi upon evaluation of the Associate Editor and Reviewers’ comments.

Brian Ye, Zhuonan Hao, Priya Shah, and Mohammad Khalid Jawed are with the Department of Mechanical & Aerospace Engineering at the University of California, Los Angeles (email: yebrian1@g.ucla.edu; znhao@g.ucla.edu; priyashah@g.ucla.edu; khalidjm@seas.ucla.edu).

* The authors contributed equally.

[†] Corresponding author: Mohammad Khalid Jawed.

This research was funded in part by the National Science Foundation under award numbers CAREER-2047663, and CMMMI-2332555.

Digital Object Identifier (DOI): see top of this page.

negative pressure to move biological waste. However, these prior works are constrained by manufacturing complexity, high costs, and limited adaptability to objects of varying sizes, such as compact and elongated shapes. In contrast, modular systems offer clear benefits, including enhanced portability, rapid deployment, and flexibility to adapt to various tasks, making them more sustainable in a wide range of applications, such as space station operations and search and rescue missions. Additionally, unlike monolithic designs where the failure of any component leads to system-wide breakdown, modular systems allow for the replacement or repair of only the affected module. This reduces downtime, resource consumption, and enhances operational continuity.

Inspired by studies on toroidal actuators, we recognize the potential for developing a modular system that leverages both radial and axial expansion – not only for gripping applications through radial contraction but also for propagation via axial expansion. Dang et al. [20] introduced a ring-shaped pneumatic actuator capable of radial contraction, demonstrating its effectiveness in gripping objects such as eggs and beakers. Hashem et al. [21] further explored this concept, showcasing its ability to grip delicate items – such as bellows, cherry tomatoes, and soft candy – by adjusting the pneumatic system’s loading conditions. Root et al. [22] utilized a hydrostatic mechanism to achieve controlled gripping, catching, and object conveyance. Zang et al. [23] presented a torus-like self-adaptive grasper capable of handling objects of unknown shapes, sizes, and softness. By adjusting the rolling direction and length of the torus skin, the system could engulf, swallow, and release objects. Perez et al. [24] developed a toroidal actuator with both axial and radial expansion; however, its radial expansion is outward rather than inward, limiting its ability to achieve internal object transport. Despite these advancements, there remains a gap in the literature regarding the use of successive radial and axial expansions to enable controlled peristaltic motion for object transport.

To bridge this gap, we propose a system that leverages sequential radial and axial deformations to enable continuous and adaptive object transport, as Figure 1 shown. Unlike conventional soft grippers that rely on discrete pick-and-place operations, our peristaltic transport system facilitates seamless handling without the need for precise positioning, making it well-suited for manipulating objects of varying shapes and sizes. The system is designed to be modular, allowing for adjustable lengths tailored to specific tasks. Its modularity ensures easy transport and assembly for rapid deployment while maintaining resilience—ensuring that the failure of a single module does not compromise the entire operation. Our contributions include:

- 1) The design of a donut-shaped actuation module, along with the development of a modular actuator system.
- 2) A real-time pressure feedback control strategy to ensure smooth object handling and transportation.

Additionally, we provide a tutorial video¹ to facilitate re-

production and publicly release all simulation data² for future research and applications.

The paper is structured as follows: Section II provides an overview of the actuator design and fabrication. Section III delves into the peristaltic transportation mechanism and its control strategies. Section IV presents the experimental and simulation results on the peristaltic actuator. Finally, Section V provides concluding remarks and future directions.

II. PERISTALTIC ACTUATOR

This section details the design and fabrication of the presented bio-inspired peristaltic actuator. The actuator features two distinct types of inflation modules: a compression module, which produces radial displacement, and a longitudinal module, which generates axial displacement. The modular design enables easy stacking of multiple units in any configuration or sequence, allowing for enhanced scalability and adaptability.

A. Design and Material Specifications

Each actuation module is composed of donut-shaped soft ring containing multiple internal air chambers, as shown in Figure 2(a), encased in a 3D-printed outer casing. To simplify fabrication, both types of actuation modules – compression and longitudinal – utilize a similar ring design as shown in Figure 2(b). The strain-limiting casing restricts the deformation of the soft ring in specific directions: the compression module is prevented from axial deformation, while the longitudinal module is constrained from radial deformation. As a result, the compression module only inflates radially to grasp an object, while the longitudinal module inflates axially to transport it along the axis of the stacked modules, hereafter referred to as the “station.” This modular approach allows for low-cost replacements in the event of partial module failures, eliminating the need for multiple specialized molds.

The inclusion of multiple air chambers is essential for promoting uniform radial inflation. Using a single air chamber may cause visible inhomogeneous deformation, resulting in a loss of axisymmetry due to the self-contact. By incorporating multiple chambers, we also minimize the risk of defects in one chamber affecting the inflation of others.

The rings are fabricated from silicone rubber (Smooth-On Ecoflex™ 00-45 Near Clear™), selected for its low cost and hyperelastic behavior with relatively low stiffness (Shore 00 hardness 45) that facilitates easy inflation. Its hyperelastic nature permits deformations over numerous cycles without permanent shape change, enabling effective pneumatic actuation and ensuring consistent performance without degradation over time. The outer casing is constructed from Thermoplastic Polyurethane (TPU) (Giantarm™ 95A TPU Filament, 1.75mm, Clear), which has a higher stiffness (Shore A hardness 95). TPU serves as a strain-limiting layer, providing the necessary structural support to withstand the weight of stacked modules in the station. Without TPU, the stacked soft rings would be unable to maintain the station’s overall shape due to their own weight.

¹<https://youtu.be/uWucfxMYyb0>

²https://github.com/StructuresComp/Peristaltic_Actuator.git

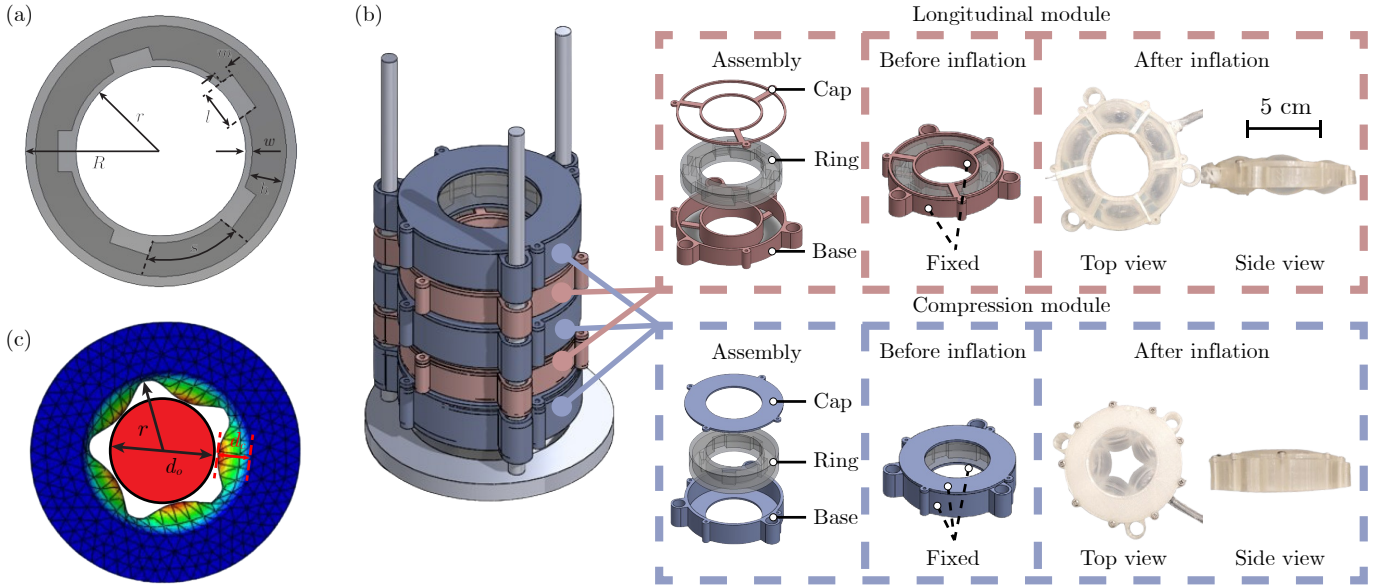


Fig. 2: Design of the actuation module. (a) Each module is donut-shaped with outer radius (R), inner radius (r), and multiple air chambers defined by length (s), width (h), spacing (l), and wall thickness (t). Chambers are interconnected by air tunnels with step height (m). (b) The actuator station consists of stacked modules. In the longitudinal module, the casing permits inflation along the top and bottom surfaces, while in the compression module, inflation is restricted to the inner surface. (c) Finite element mesh of the actuation module, showing the maximum radial inflation displacement (d_c). The object is characterized by its maximum cross-sectional dimension d_o .

TABLE I: Geometrical parameters

Description	Symbol	Value	Unit
Outer radius	R	40	mm
Inner radius	r	25	mm
Step height	m	4	mm
Chamber spacing	l	12	mm
Wall thickness	w	2	mm
Chamber length	s	28.8	mm
Chamber width	h	10	mm
Object dimension	d_o	20 – 50	mm

B. Fabrication and Assembly

The base and cap of the TPU casings, are printed using a 3D printer (Original Prusa™ i3 MK3S+ 3D Printer). Following this, we fabricate the soft rings through a step-by-step casting and curing process, as illustrated in Figure 3. To prepare the mixture, combine Part A and Part B of Ecoflex silicone in a 1:1 ratio by weight and mix thoroughly by hand using a craft stick for three minutes at room temperature (23°C). To fabricate the internal air chambers, the ring mold is designed with separate top and bottom sections. Once the two sections are glued together later in the process, the empty spaces in each section will combine to form the air chambers.

First, the mixture is poured into the bottom section to form the bottom surface and walls. To eliminate air bubbles from the mixture, the entire assembly (mixture and mold) is placed under vacuum at 100 kPa for two minutes. As the mixture begins to solidify after a few minutes, a small hole is punctured in the outer surface to create an opening for the tubing connector used for inflation. The tubing connector is then attached, and additional Ecoflex mixture is used to seal the connection between the tubing and the bottom section. After approximately twenty minutes, the mixture starts to take

on a solid form. At this stage, but before it fully cures (which can take several hours), the bottom part is placed onto the base of the TPU casing.

Additional Ecoflex mixture is prepared and poured into the mold for the top section. Vacuum is again used to remove air bubbles. The partially cured bottom section is then positioned directly onto the still-curing top section. This assembly is allowed to cure at room temperature (23°C) for four hours, ensuring a strong bond between the two parts and the proper sealing of the air chambers. By allowing the top section to cure simultaneously with the bottom, we strengthen the mechanical bond between the two surfaces, enhancing the overall durability and performance of the actuator module.

The final stage involves connecting the TPU cap to the base using mechanical screws. Once each actuation module is completed, we stack them in the sequence of compression, longitudinal, compression, and so on, to construct an integrated actuator station. To ensure alignment among multiple modules, 3D-printed guide rails are used.

C. Simulation Framework

The inflation behavior of the actuator was simulated using Finite Element Analysis (FEA) in Abaqus™ (Academic Edition on UCLA Hoffman2 cluster). The simulation results guided the selection of optimal geometric parameters for the experimental setup, helping to minimize material waste, fabrication costs, and time-consuming trial-and-error processes. The final geometric parameters used in the experiments are detailed in Table I, and a more in-depth discussion of the simulation results will be provided in Section IV.

The geometry in Figure 2(c) was discretized using tetrahedral mesh elements (C3D10), with a 3D model created

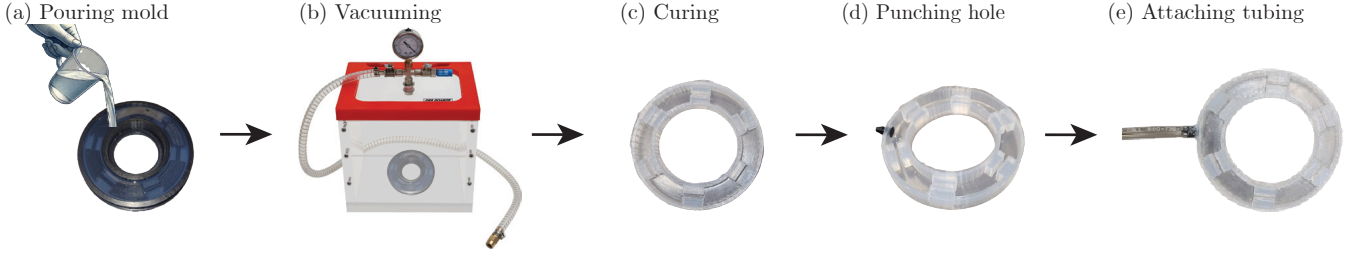


Fig. 3: Fabrication process of the actuation module. (a) Pouring silicone material into the mold. (b) Removing air bubbles using a vacuum chamber. (c) Allowing the silicone to cure. (d) Creating openings on the outer surface for connectors and tubing. (e) Attaching tubing to finalize the assembly. Steps (a) and (b) are repeated for the upper mold, which is then cured together with the completed bottom mold.

in SolidWorks™ and imported into Abaqus™. The mesh included 49,736 nodes and 29,686 elements. A hyperelastic Mooney-Rivlin model was used, with nonlinear geometry enabled in the software. Material properties were approximated for Ecoflex silicone (Shore 00 hardness 45), assigning a Young's modulus of 100 kPa [25] and a Poisson's ratio of 0.44 (selected to avoid numerical instability from a Poisson ratio of 0.5 while remaining close to incompressible behavior). The model's coefficients were $C_{10} = C_{01} = 8620.69$ Pa and $D_1 = 2.4 \times 10^{-6}$ Pa [26]. A pressure load of 15 kPa, measured experimentally, was applied to simulate the inflation process. The ratio of the two parameters C_{01} and C_{10} was assumed to be one; we observed that varying this ratio between 0.5 and 10 had a negligible effect on our results.

The boundary conditions were applied differently for the two modules. For the longitudinal module, nodes on the side walls were constrained using an encastre boundary condition, meaning they were fully fixed in place with no translation or rotation allowed, to prevent any deformation. The nodes on the top and bottom walls were free to deform under the applied pressure. In contrast, for the compression module, the nodes on the top and bottom walls, as well as the nodes on the outer surface of the side walls, were constrained. However, the nodes on the inner side walls were free.

For the purposes of numerical simulations, keep in mind that the primary function of the longitudinal module is to provide upward movement through repeated actuation cycles. The total displacement of the object is simply the product of the upward movement per cycle times the number of cycles. Since this is a prototype design study, our primary focus is not on power consumption and efficiency at this stage but rather on feasibility. We can simply increase the number of cycles to achieve the desired movement. In contrast, the compression module is crucial for grasping the object securely during transport. A stronger grasp allows the system to handle a wider variety of objects. Therefore, the focus of our modeling efforts is on refining the geometric parameters of the compression module to maximize its grasping effectiveness. To describe the inflation behavior, we introduce normalized inflation \bar{d}_c , defined as the ratio of the maximum radial inflation displacement d_c to the inner radius r of the compression module, as Figure 2(c). In simulation, d_c represents the maximum deformation of the nodes positioned along the inner side wall. Additionally, to characterize the object dimension d_o – the maximum cross-sectional dimension – in the context of the

system, we use the normalized dimension \bar{d}_c , defined as the ratio of d_o to the inner radius r .

D. Experimental Setup

The overall setup relies on sequential inflation and deflation of the modules to transport an object, as detailed later in Section III. This process requires precise pressure sensing from each actuation module, allowing the system to detect when the object is in contact with the current module through variations in pressure signals. As shown in Figure 4, the system to accomplish this objective includes an air pump and vacuum, air valves, pressure sensors, and a microcontroller, as a closed-loop pneumatic control system.

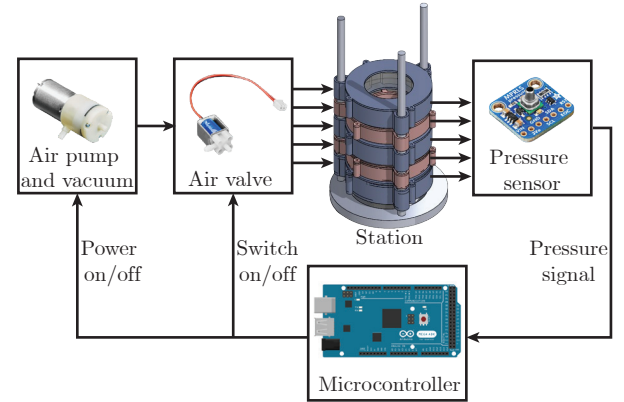


Fig. 4: Hardware setup. The actuator station incorporates an air pump and vacuum, air valves, pressure sensors, and a microcontroller, providing both sensing and control capabilities.

The pressure sensors (Adafruit™ MPRLS Ported Pressure Sensor Breakout - 0 to 25 PSI) monitor the internal pressures of each actuation module in real time, providing data for feedback loops to control inflation and deflation. This pressure data is transmitted to the microcontroller (Arduino™ Mega 2560 Rev3), which manages airflow supplied by the air pump (Adafruit™ Air Pump and Vacuum DC Motor - 4.5 V and 2.5 LPM - ZR370-02PM).

Following a control sequence outlined later in Section III, the air valves (Adafruit™ 6V Air Valve with 2-pin JST XH Connector - FA0520E) precisely regulate airflow into and out of the individual actuation module.

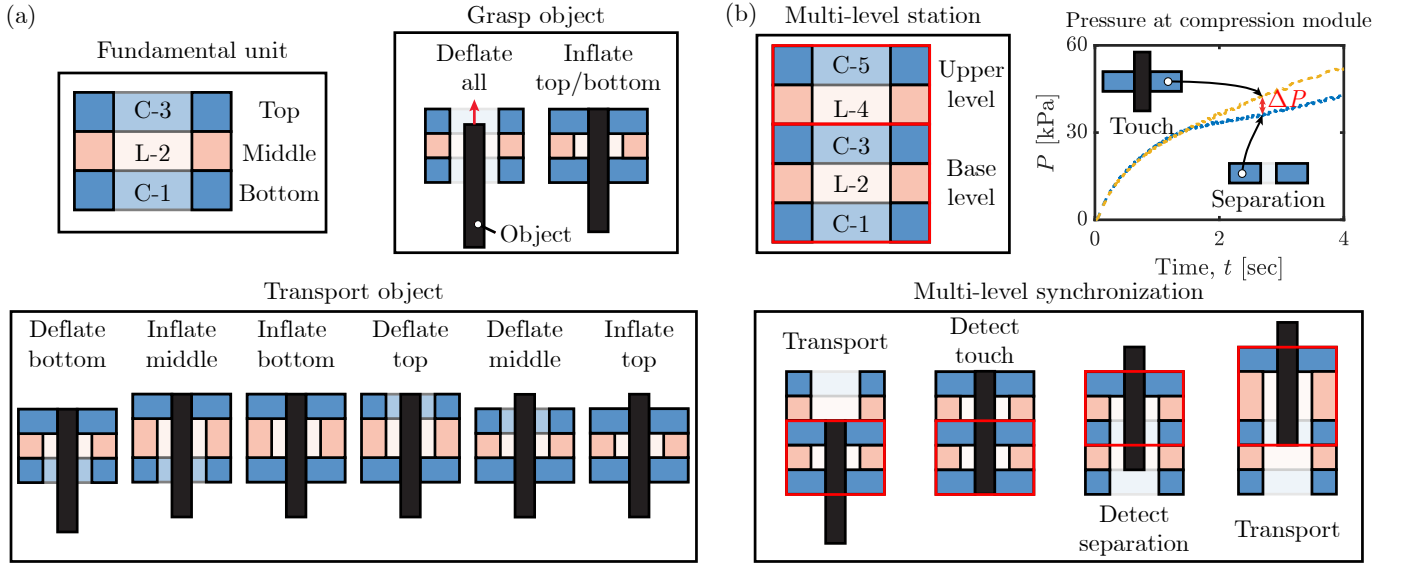


Fig. 5: Control of peristaltic transportation. (a) The fundamental unit, composed of two compression modules at the top and bottom with a longitudinal module in the middle, enables object grasp and transport through sequence-based control of the actuation modules. (b) The multi-level station, where synchronization is achieved by acquiring pressure signal differences ΔP between the adjacent compression modules. Actuation timing is adjusted based on whether the object is grasped by the upper level modules.

III. PERISTALTIC TRANSPORTION

The peristaltic transportation mechanism in our actuator utilizes sequential inflation and deflation of individual actuation modules to enable controlled movement and object manipulation. This section highlights two key aspects of the system's operation. First, the fundamental unit, consisting of three actuation modules, performs basic tasks such as object grasping and transport through sequential control. Second, we examine the concept of synchronization as additional modules are stacked, creating a multi-level structure that necessitates coordinated control across different levels. This coordination ensures consistent and continuous behavior, facilitated by a closed-loop control system.

A. Sequence-Based Control of Fundamental Unit

As shown in Figure 5(a), The fundamental unit capable of peristaltic transportation consists of three actuation modules: a compression module at the bottom (C-1), a longitudinal module in the middle (L-2), and another compression module at the top (C-3). This configuration allows for sequential inflation and deflation to achieve object grasp and transport.

To begin, both the top and bottom compression modules are inflated to securely grip the object. Next, to transport the object, the bottom compression module is deflated while the middle longitudinal module inflates, generating an effective axial displacement for the object. Once the middle module has displaced the object, the bottom module is inflated again to re-grasp, and the top module is deflated. Finally, the middle module is deflated, the top module is re-inflated, and the process is repeated. This cyclical sequence of inflating and deflating the modules ensures that the object is progressively transported through the fundamental unit.

B. Pressure Feedback Control of Multi-Level Station

As the system is scaled by stacking additional modules – commonly required in practical applications for varying transportation distances – it becomes critical to implement a control strategy that adjusts actuation based on the object's position along the stacked modules. In the multi-level station, as shown in Figure 5(b), the base level functions as a fundamental unit. When additional longitudinal-compression modules (L-4, C-5, etc.) are stacked on top of the base, higher levels are formed. The primary challenge is coordinating the actuation of these upper levels to ensure smooth object transport. Since the object moves from bottom to top, the base level is actuated first. However, determining the optimal timing to activate the upper levels as the object approaches remains a critical problem.

To address this, we utilize pressure signals from sensors integrated into each compression module. When an object contacts the air chamber, the pressure increases more rapidly, exhibiting a higher rate of change compared to when no object is present. During each actuation period, we take multiple pressure measurements at short time intervals. If the pressure change rate exceeds a predefined threshold – established based on inflation without an object – we determine that the current compression module is in contact with the object. Upon detecting contact in an upper compression module, we deactivate the lower module and designate the upper and middle modules as the fundamental unit to transport. By monitoring the pressure change rate in real time, we dynamically adjust the actuation sequence to facilitate smooth and continuous upward transport.

IV. RESULTS AND DISCUSSION

In this section, we present simulation results on actuator design and experimentally evaluate grasping and transportation performance. First, we use finite element analysis (FEA) to explore the geometric parameter space of the compression

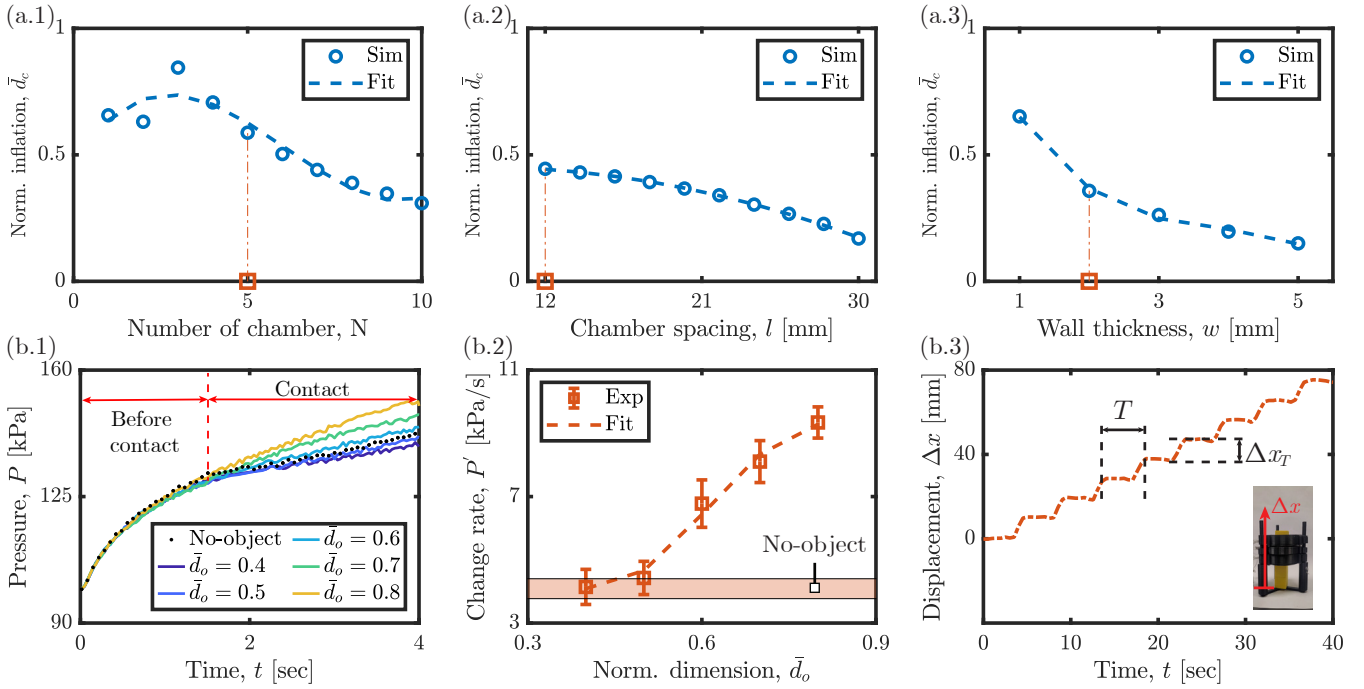


Fig. 6: Evaluation of the actuator design. (a) Simulation of the geometrical design parameters for the compression module. Blue circles indicate simulation results with a fitted curve. (a.1) The normalized inflation \bar{d}_c plotted against the number of chambers N . (a.2) The normalized inflation \bar{d}_c plotted against the chamber spacing l . (a.3) The normalized inflation \bar{d}_c plotted against the wall thickness w . Red squares highlight the final design parameters selected for the experimental setup: $N = 5$, $l = 12$ mm, and $w = 2$ mm. (b) Experimental evaluation of object grasping and transport. (b.1) Chamber pressure P of compression module over time t when grasping cylinder objects of different normalized diameter \bar{d}_o , compared to the no-object case. Each dimension was tested five times, and only one representative curve for each case is shown for clarity. (b.2) Pressure change rate P' of compression module during contact phase, plotted against normalized dimension \bar{d}_o . Error bars indicate the mean and variance across multiple experimental trials. (b.3) Object displacement Δx over time t , with the period of the inflation-deflation cycle T corresponding to displacement Δx_T .

module. Based on these findings, we determine the optimal parameters for the experimental setup to achieve effective actuation. We then conduct inflation tests to characterize object transport and assess the range of object sizes suitable for grasping and movement. Finally, we examine the pressure-based multi-level synchronization strategy and demonstrate how different module sequences impact transportation speed.

A. Parameter Space for Actuation Module Design

The compression module plays a critical role in object grasping. In Figure 2(c), we use the radial inflation displacement, d_c , to characterize the range of object dimension d_o that can be grasped, i.e., $d_o/2 \in (r - d_c, r)$. Assisted by FEA, we investigate how geometric parameters of the ring influence the radial inflation displacement. Detailed simulation results can be found in the supplementary video.

To comprehensively describe the geometry of the compression ring, we consider seven key parameters, as illustrated in Figure 2(a). The step height m and chamber width h define the dimensions of the air tunnel and chambers in the direction perpendicular to the airflow, affecting how efficiently air can inflate between the chambers. However, given the already small system dimensions, there is limited flexibility in adjusting these parameters without risking airflow impedance. As a result, we exclude these parameters from further investigation, selecting values that balance ease of fabrication with effective

airflow. While the outer radius R and inner radius r define the critical dimensions, we study how the remaining parameters impact the inflation behavior, characterized by the normalized inflation \bar{d}_c .

The variables that define the air chamber distribution around the ring include the chamber length l , chamber spacing s , and the number of air chambers N . These parameters are interrelated and governed by the following relationship

$$(s + l) \times N = \pi(R + r).$$

Therefore, we investigate how variations in N and l influence inflation, with s coupled to these parameters while R and r remain fixed. As shown in Figure 6(a.1), we observe that \bar{d}_c does not monotonically change with N . When $N = 1$ or 2 , \bar{d}_c is lower than for $N = 3$ due to severe self-contact as discussed before. As the number of chambers increases, \bar{d}_c decreases because the increased air chamber volume inflates less under a constant pressure loading. Additionally, as shown in Figure 6(a.2), we observe that as the spacing l increases, \bar{d}_c decreases. This is because chambers that are spaced too sparsely inflate more slowly, resulting in less efficient inflation-deflation cycles.

Furthermore, wall thickness is essential in determining surface stiffness. Thinner walls inflate more easily, as shown in Figure 6(a.3), but they are also more susceptible to damage, such as bulging or bursting under pressure.

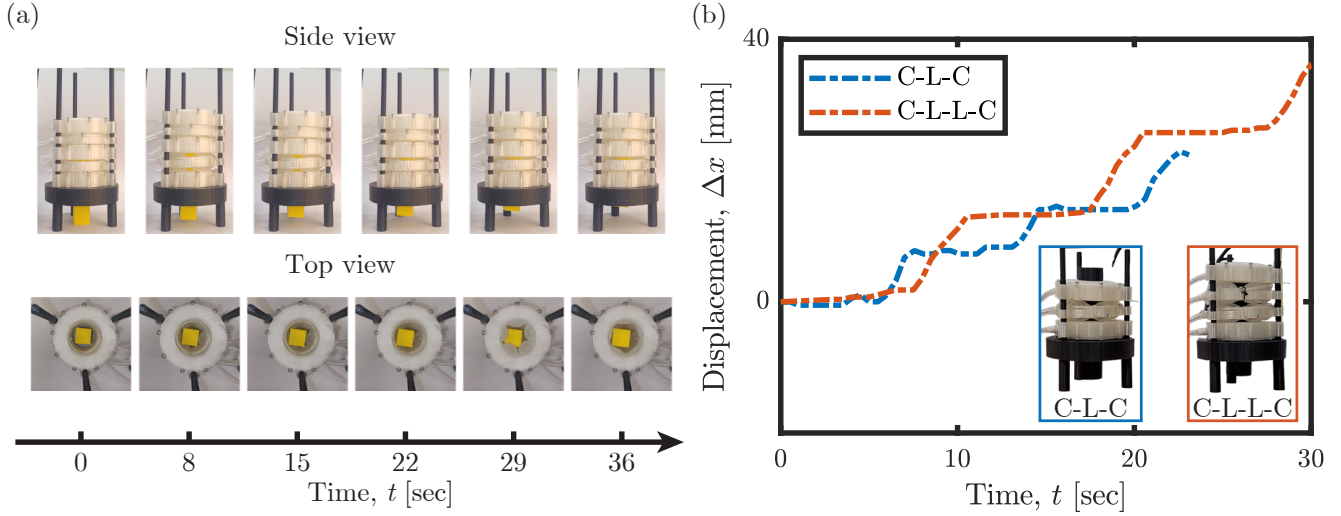


Fig. 7: Demonstration of the modular features on system variation. (a) Multi-level synchronization in object transportation. (b) Module sequence on object transportation performance during three periods, i.e., C-L-C of 1.00 ± 0.11 mm/s and C-L-L-C of 1.23 ± 0.06 mm/s.

To balance between structural robustness and inflation performance, we selected a set of appropriate geometric parameters, marked as red squares in Figure 6(a), with $s = 28$ mm, $l = 12$ mm (corresponding to $N = 5$), and $w = 2$ mm. These parameters were used consistently across all the following experiments.

B. Object Grasping and Transportation

For effective grasping, the object dimension d_o must not exceed the inner diameter of the actuation ring. If d_o is too small, the inflated chamber of the compression module may not make sufficient contact. Conversely, if d_o is too close to the inner diameter, contact is ensured, but inflation may be restricted, potentially damaging the air chamber.

To determine the effective range of object dimensions, we use cylinders with diameter d_o , ranging from 0.4 to 0.8 times the inner diameter of the actuation ring. As shown in Figure 6(b.1), upon inflation, we observe an initial transition phase – termed the “before contact” stage – lasting about 1.5 seconds, during which the pressure curves follow similar trends regardless of the object’s dimensions. Following this, in the “contact” stage, larger dimensions result in a more rapid pressure change rate due to increased squeezing.

To facilitate comparison, we compute the slope of each pressure curve during the “contact” stage, represented as the pressure change rate P' . In Figure 6(b.2), we present P' for varying cylinder dimensions d_o . Each dimension was tested five times to enhance result reliability, with error bars indicating variability. The baseline, shown as the orange band, is established with no object present. We find that when $\bar{d}_o = 0.4$, P' falls within the band zone, indicating that the compression module cannot reliably detect the presence of an object through pressure change rate, although it may still grasp it. As a result, the effectiveness of multi-level synchronization through pressure feedback would be limited. However, this minimal object dimension may vary depending on different module design parameters.

Additionally, to evaluate the transportation performance, we use a fundamental unit to move a soft cuboid with $\bar{d}_o = 0.708$ (squared cross-section with side length of 20 mm) and mass of $m = 5$ g and track its displacement Δx over time. Due to the nature of sequential control, the object only moves when the longitudinal module is inflated. As shown in Figure 6(b.1), the object exhibits periodic upward movement, characterized by a period $T = 4.5$ s (representing the time of an inflation-deflation cycle of the fundamental unit) and a corresponding displacement $\Delta x_T = 9.5$ mm (the inflation distance of the longitudinal module). The average transportation speed is simply $v_o = \Delta x_T / \Delta T \approx 2.08 \pm 0.07$ mm/s.

C. Pressure-Based Synchronization

Leveraging the advantage of modular design, the modules can be easily stacked in varying lengths to form a multi-level station, allowing for the transportation of objects over different distances. Using a pressure-based control strategy, we demonstrate its ability to transport objects smoothly and continuously across different levels.

As shown in Figure 7(a), we use a two-level station to transport the soft cuboid with $\bar{d}_o = 0.708$. At $t = 0$, the object is in contact with compression modules C-1 and C-3. Once C-3 inflates, we also inflate C-5 and monitor its chamber pressure. The inflation-deflation cycle period, T , for the fundamental units is 4.5 s. During the first four cycles from $t = 0$ to $t = 18$ s, the pressure in C-5 remains similar to its no-object condition, with $P' \approx 4.33$ kPa/s. The upper longitudinal module L-4 remains inactive, and the fundamental unit consisting of C-1, L-2, and C-3 continues to operate. However, at $t = 22$ s, the pressure in C-5 suddenly increases to 8.48 kPa/s, approximately doubling, signaling the detection of the object. The system then activates the upper level, which includes L-4 and C-5, to work in tandem with C-3, while deactivating C-1 and L-2. This process continues, activating additional levels in sequence until the object reaches the top. This approach ensures smooth, synchronized transport across the stacked

modules. Further details of the transportation process can be found in the supplementary video.

D. Module Sequence on Transportation Speed

As another benefit of the modular design, the system allows for varying actuation module sequences. The fundamental units consist of two compression modules and one longitudinal module for transportation. However, by inserting additional longitudinal modules, we can study how the module sequence affects transportation speed.

As shown in Figure 7(b), compared with the conventional C–L–C configuration, the C–L–L–C configuration changes the period T (from 9 s to 13 s) and corresponding displacement Δx_T (from 7.5 mm to 13 mm). On one hand, T increases, as we use one pump to inflate two longitudinal modules, which consumes the similar energy. Although the inflation time of C–L–L–C configuration is longer, it does not double as C–L–C configuration, only increasing by about 1.5 times. On the other hand, Δx_T for C–L–L–C configuration almost doubles, since both longitudinal modules contribute to displacement. Overall, the transportation speed of C–L–L–C configuration increases by 1.2 times compared to the C–L–C configuration, achieving higher speed by simply reordering the actuation module sequence. Further details on the configuration comparison are available in the supplementary video.

V. CONCLUSIONS

In conclusion, this study presents a bio-inspired pneumatic modular actuator designed for peristaltic transport, highlighting its potential for object manipulation of varying shape and size. By developing distinct actuation modules – compression and longitudinal by either stack number or sequence – we have established a scalable, adaptable architecture that allows for varying transportation tasks. The integration of pressure feedback mechanisms enhances the system’s ability to detect object position.

Future work will focus on systematically exploring the parameter space of both longitudinal and compression modules while optimizing efficiency through adjustments to the actuation period and configuration sequence. Additionally, efforts will be made to seamlessly integrate the system with existing robotic platforms, such as manipulators, to handle fragile objects like coral reefs and strawberries, thereby expanding its practical applications.

REFERENCES

- [1] K. S. Patel and A. Thavamani, “Physiology, peristalsis,” in *StatPearls* [Internet], StatPearls Publishing, 2023.
- [2] K. J. Quillin, “Kinematic scaling of locomotion by hydrostatic animals: ontogeny of peristaltic crawling by the earthworm *lumbricus terrestris*,” *Journal of Experimental Biology*, vol. 202, no. 6, pp. 661–674, 1999.
- [3] Y. Tanaka, K. Ito, T. Nakagaki, and R. Kobayashi, “Mechanics of peristaltic locomotion and role of anchoring,” *Journal of the Royal Society Interface*, vol. 9, no. 67, pp. 222–233, 2012.
- [4] A. Bursian, “Structure of autorhythmic activity of contractile systems,” *Journal of Evolutionary Biochemistry and Physiology*, vol. 48, pp. 219–235, 2012.
- [5] J. G. Brasseur, “A fluid mechanical perspective on esophageal bolus transport,” *Dysphagia*, vol. 2, pp. 32–39, 1987.
- [6] A. Góra, D. Pliszka, S. Mukherjee, and S. Ramakrishna, “Tubular tissues and organs of human body—challenges in regenerative medicine,” *Journal of nanoscience and nanotechnology*, vol. 16, no. 1, pp. 19–39, 2016.
- [7] T. Nakamura and T. Iwanaga, “Locomotion strategy for a peristaltic crawling robot in a 2-dimensional space,” in *2008 IEEE International Conference on Robotics and Automation*, pp. 238–243, IEEE, 2008.
- [8] N. Saga and T. Nakamura, “Development of a peristaltic crawling robot using magnetic fluid on the basis of the locomotion mechanism of the earthworm,” *Smart materials and structures*, vol. 13, no. 3, p. 566, 2004.
- [9] A. Kandhari, Y. Wang, H. J. Chiel, R. D. Quinn, and K. A. Daltorio, “An analysis of peristaltic locomotion for maximizing velocity or minimizing cost of transport of earthworm-like robots,” *Soft robotics*, vol. 8, no. 4, pp. 485–505, 2021.
- [10] S. Seok, C. D. Onal, K.-J. Cho, R. J. Wood, D. Rus, and S. Kim, “Meshworm: a peristaltic soft robot with antagonistic nickel titanium coil actuators,” *IEEE/ASME Transactions on mechatronics*, vol. 18, no. 5, pp. 1485–1497, 2012.
- [11] I. Sensory, “A review on the food digestion in the digestive tract and the used in vitro models,” *Current research in food science*, vol. 4, pp. 308–319, 2021.
- [12] D. Trivedi, C. D. Rahn, W. M. Kier, and I. D. Walker, “Soft robotics: Biological inspiration, state of the art, and future research,” *Applied bionics and biomechanics*, vol. 5, no. 3, pp. 99–117, 2008.
- [13] D. Rus and M. T. Tolley, “Design, fabrication and control of soft robots,” *Nature*, vol. 521, no. 7553, pp. 467–475, 2015.
- [14] J. Liu, P. Li, and S. Zuo, “Actuation and design innovations in earthworm-inspired soft robots: A review,” *Frontiers in Bioengineering and Biotechnology*, vol. 11, p. 1088105, 2023.
- [15] S. Dirven, F. Chen, W. Xu, J. E. Bronlund, J. Allen, and L. K. Cheng, “Design and characterization of a peristaltic actuator inspired by esophageal swallowing,” *IEEE/ASME Transactions on Mechatronics*, vol. 19, no. 4, pp. 1234–1242, 2013.
- [16] Y. Peng, H. Nabae, Y. Funabara, and K. Suzumori, “Peristaltic transporting device inspired by large intestine structure,” *Sensors and Actuators A: Physical*, vol. 365, p. 114840, 2024.
- [17] Y. Peng, H. Nabae, Y. Funabara, and K. Suzumori, “Controlling a peristaltic robot inspired by inchworms,” *Biomimetic Intelligence and Robotics*, vol. 4, no. 1, p. 100146, 2024.
- [18] S. Uzawa, H. Kumamoto, C. Yamazaki, M. Okui, and T. Nakamura, “Development of peristaltic transfer system to transport feces in space: proposal of driving method using pressure difference in peristaltic pump,” *IEEE Access*, vol. 10, pp. 128399–128407, 2022.
- [19] M. Kawano, S. Uzawa, C. Yamazaki, and T. Nakamura, “Development of a peristaltic flexible transfer system for transporting feces under microgravity: Construction and validation of transport models,” in *2024 IEEE/RSJ International Conference on Intelligent Robots and Systems (IROS)*, pp. 4527–4533, IEEE, 2024.
- [20] Y. Dang, M. Stommel, L. K. Cheng, and W. Xu, “A soft ring-shaped actuator for radial contracting deformation: Design and modeling,” *Soft robotics*, vol. 6, no. 4, pp. 444–454, 2019.
- [21] R. Hashem, M. Stommel, L. K. Cheng, and W. Xu, “Design and characterization of a bellows-driven soft pneumatic actuator,” *IEEE/ASME Transactions on Mechatronics*, vol. 26, no. 5, pp. 2327–2338, 2020.
- [22] S. E. Root, D. J. Preston, G. O. Feifke, H. Wallace, R. M. Alcoran, M. P. Nemitz, J. A. Tracz, and G. M. Whitesides, “Bio-inspired design of soft mechanisms using a toroidal hydrostat,” *Cell Reports Physical Science*, vol. 2, no. 9, 2021.
- [23] H. Zang, B. Liao, X. Lang, Z.-L. Zhao, W. Yuan, and X.-Q. Feng, “Bionic torus as a self-adaptive soft grasper in robots,” *Applied Physics Letters*, vol. 116, no. 2, 2020.
- [24] E. Perez-Guagnelli, J. Jones, and D. D. Damian, “Hyperelastic membrane actuators: Analysis of toroidal and helical multifunctional configurations,” *Cyborg and Bionic Systems*, 2022.
- [25] D.-H. Kim, N. Lu, R. Ma, Y.-S. Kim, R.-H. Kim, S. Wang, J. Wu, S. M. Won, H. Tao, A. Islam, et al., “Epidermal electronics,” *science*, vol. 333, no. 6044, pp. 838–843, 2011.
- [26] T. Gopesh and J. Friend, “Facile analytical extraction of the hyperelastic constants for the two-parameter mooney–rivlin model from experiments on soft polymers,” *Soft Robotics*, vol. 8, no. 4, pp. 365–370, 2021.